ACS NANO

www.acsnano.org

ARTICLE

Reconfigurable Manipulation of Oxygen Content on Metal Oxide Surfaces and Applications to Gas Sensing

Gyuweon Jung, Suyeon Ju, Kangwook Choi, Jaehyeon Kim, Seongbin Hong, Jinwoo Park, Wonjun Shin, Yujeong Jeong, Seungwu Han, Woo Young Choi, and Jong-Ho Lee*

Cite This: *ACS Nano* 2023, 17, 17790−17798

Read Online

ACCESS | Metrics & More | Article Recommendations | Supporting Information

ABSTRACT: **Oxygen vacancies and adsorbed oxygen species on metal oxide surfaces play important roles in various fields. However, existing methods for manipulating surface oxygen require severe settings and are ineffective for repetitive manipulation. We present a method to manipulate the amount of surface oxygen by modifying the oxygen adsorption energy by electrically controlling the electron concentration of the metal oxide. The surface oxygen control ability of the method is verified using first-principles calculations based on density functional theory (DFT), X-ray photoelectron spectroscopy (XPS), and electrical resistance analysis. The presented method is implemented by fabricating oxide thin film transistors with embedded microheaters. The method can reconfigure the oxygen vacancies on the In_2O_3, SnO_2, and IGZO surfaces so that specific chemisorption dominates. The method can selectively increase oxidizing (e.g., NO and NO) and reducing gas (e.g., H_2S, NH_3, and CO) reactions by electrically controlling the metal oxide surface to be oxygen vacancy-rich or adsorbed oxygen species-rich. The proposed method is applied to gas sensors and overcomes their existing limitations. The method makes the sensor insensitive to one gas (e.g., H_2S) in mixed-gas environments (e.g., NO_2+H_2S) and provides a linear response (R^2 = 0.998) to the target gas (e.g., NO_2) concentration within 3 s. We believe that the proposed method is applicable to applications utilizing metal oxide surfaces.**

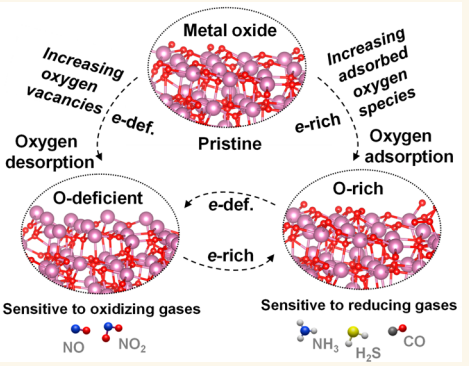

KEYWORDS: *oxygen vacancies, adsorbed oxygen species, gas sensors, metal oxides, gas mixtures identification, chemisorption, density functional theory*

INTRODUCTION

Metal oxides (MOXs) have received considerable attention for a variety of applications such as electronics, catalysis, energy conversion, and gas sensing.[1−6] In these applications, oxygen vacancies (OVs) and adsorbed oxygen species (AOSs, e.g., $O_2^-{}_{ads}$ and $O^-{}_{ads}$) on the surface of MOX have played important roles.[1−10] Particularly, since the discoveries that surface OVs serve as gas adsorption sites and that AOSs promote gas reactions,[10,11] surface AOS and OV control become vital in gas sensing applications.[10,12,13] The surface oxygen content (amount of OV and AOS) of MOXs has been modified utilizing techniques such as high-energy particle bombardment,[14] high-temperature sintering,[15] ion doping,[16] and heterostructures.[17] However, most existing modulation techniques necessitate harsh conditions such as high temperature and high vacuum, and once the oxygen content has been controlled, it is very difficult to readjust them.[10,12,14−19]

In this study, we present an electrical approach for manipulating the surface OVs and AOSs of MOXs. The oxygen adsorption energy is controlled by modulating the carrier concentration of the MOX using an electric field, and the surface oxygen content can be repeatedly tuned. To implement the proposed method, we fabricated oxide thin film transistors with embedded microheaters (Figures 1(a), S1, and S2). We demonstrate that the quantity of OV and AOS on the surface of MOX could be adjusted using X-ray photoelectron spectroscopy (XPS), first-principles calculations based on density functional theory (DFT), electrical resistance analysis, and

Received: April 4, 2023
Accepted: August 18, 2023
Published: August 23, 2023

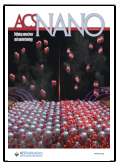

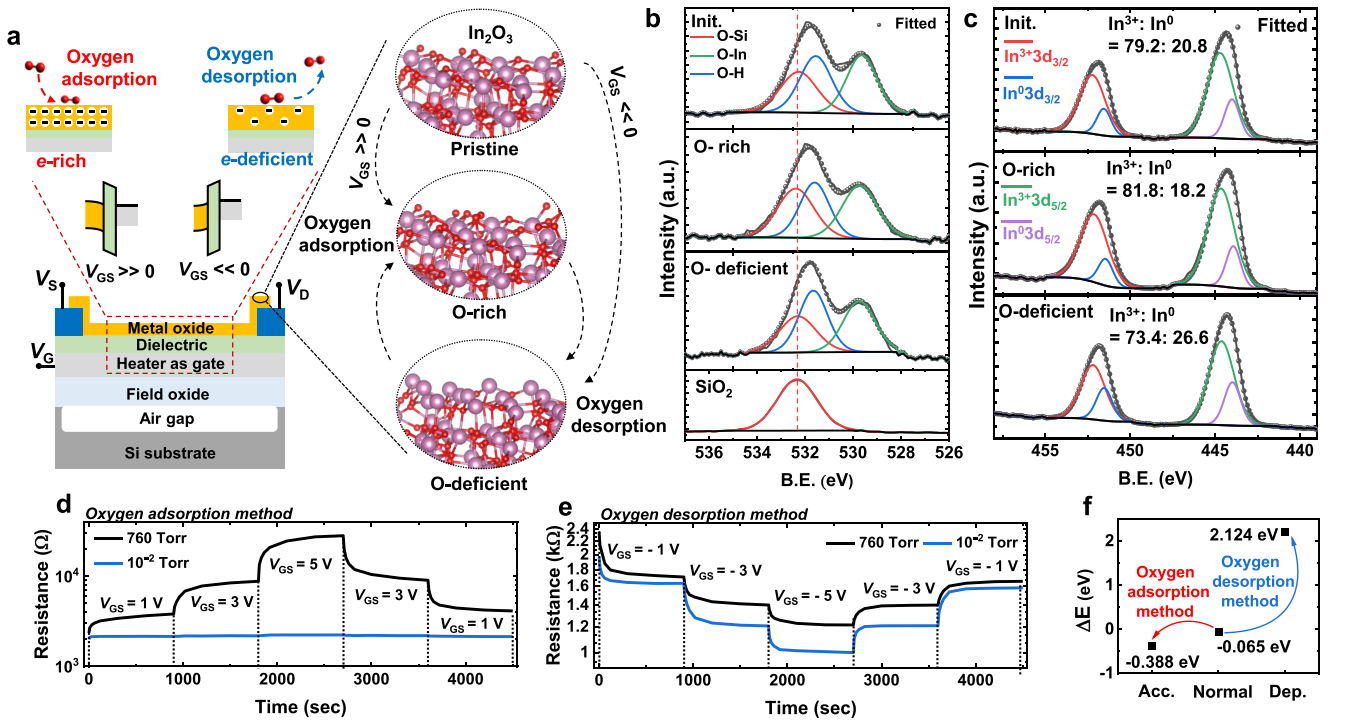

Figure 1. Reconfigurable surface oxygen manipulation method for MOX. (a) Schematic images of the band diagram, electron concentration, and enlarged surface of the In_2O_3 device when a positive or negative voltage is applied to V_{GS}. (b) High-resolution O_{1s} core level XPS spectra of the In_2O_3 device and the SiO_2 dielectric layer. The four spectra from top to bottom are the O 1s XPS spectra of the initial In_2O_3 device, the In_2O_3 device after the oxygen adsorption method, the In_2O_3 device after the oxygen desorption method, and the SiO_2 layer, respectively. (c) High-resolution In_{3d} core level XPS spectra of the In_2O_3 device. The three spectra from top to bottom are the In 3d XPS spectra of the initial In_2O_3 device, the In_2O_3 device after the oxygen adsorption method, and the In_2O_3 device after the oxygen desorption method, respectively. Electrical resistance changes in the In_2O_3 device with the (d) oxygen adsorption and (e) desorption methods at 240 °C. (f) Binding energy (ΔE) of oxygen to normal, electron-depleted, and electron-accumulated In_2O_3 calculated by DFT.

charge-transfer-based gas sensor operation. We show the performance of the proposed method using In_2O_3 as a representative, known for its high controllability of oxygen vacancies,[7,8,20] and demonstrate the applicability of the method using SnO_2 and indium gallium zinc oxide (IGZO). In addition, we show that the proposed method can manipulate MOX surfaces to the desired states independent of long-term gas interactions.

OVs and AOSs significantly influence redox reactions on MOX surfaces.[21−24] By making the MOX surface an O-deficient (OV-rich) or an O-rich (AOS-rich), we present a technique for manipulating chemisorption properties such as charge transfer and adsorption energy. We show the efficacy of the suggested technique using NO_2 and H_2S gases, typical oxidizing and reducing gases for MOX.[25] We demonstrate the effect of the proposed method by sensing the surface-gas reaction by using the fabricated devices. In other words, we regard the fabricated devices as conductometric gas sensors and obtain surface reaction information using the sensor signals. Note that gas sensors are used in a wide range of applications and have received a lot of attention.[26−29] Due to the unique construction of the devices, which utilizes a microheater as a gate, the suggested technique yields exceptional gas sensing performance. Intriguingly, the proposed method shows the possibility of solving chronic problems of MOX-based gas sensors (non-linearity, gas cross-sensitivity, slow gas identification time, and long-term reliability).[6,10,30,31] We show that making MOX surfaces either O-deficient or O-rich can selectively enhance the reactivity of gas molecules using OV as active sites or those using AOS as active sites, respectively. By precisely adjusting the MOX surface, MOX-based gas sensors can achieve a linear response and near real-time gas identification even in a mixed gas (NO_2 + H_2S + air) environment.

RESULTS AND DISCUSSION

Surface Oxygen Manipulation. Due to the ubiquitous availability of oxygen in the actual environment, oxygen molecules actively interact with MOX surfaces. We present a reconfigurable method for controlling the quantity of surface oxygen in MOX. When the electron concentration of MOX increases or decreases by an electric field at a high temperature (e.g., 240 °C), either more oxygen or less oxygen can be adsorbed on the modified surface relative to the pristine condition (Figure 1(a)). The electric field is controlled by biasing the heater as a gate. When a positive or negative voltage is applied to the gate, the carrier concentration of MOX increases and decreases; the surface oxygen concentration increases and decreases, respectively.

Point XPS is performed after applying the proposed oxygen adsorption/desorption method to the In_2O_3 device. Due to the limited resolution of point XPS analysis, the surface information on the SiO_2 dielectric layer and the In_2O_3 device is obtained simultaneously (Figure 1(b)). As a reference, the O_{1s} XPS peak of the SiO_2 dielectric layer is obtained (bottom of Figure 1(b)). The O_{1s} XPS peaks obtained from the device are then divided into peaks originating from the SiO_2 and In_2O_3 films. The O_{1s}

https://doi.org/10.1021/acsnano.3c03034
ACS Nano 2023, 17, 17790−17798

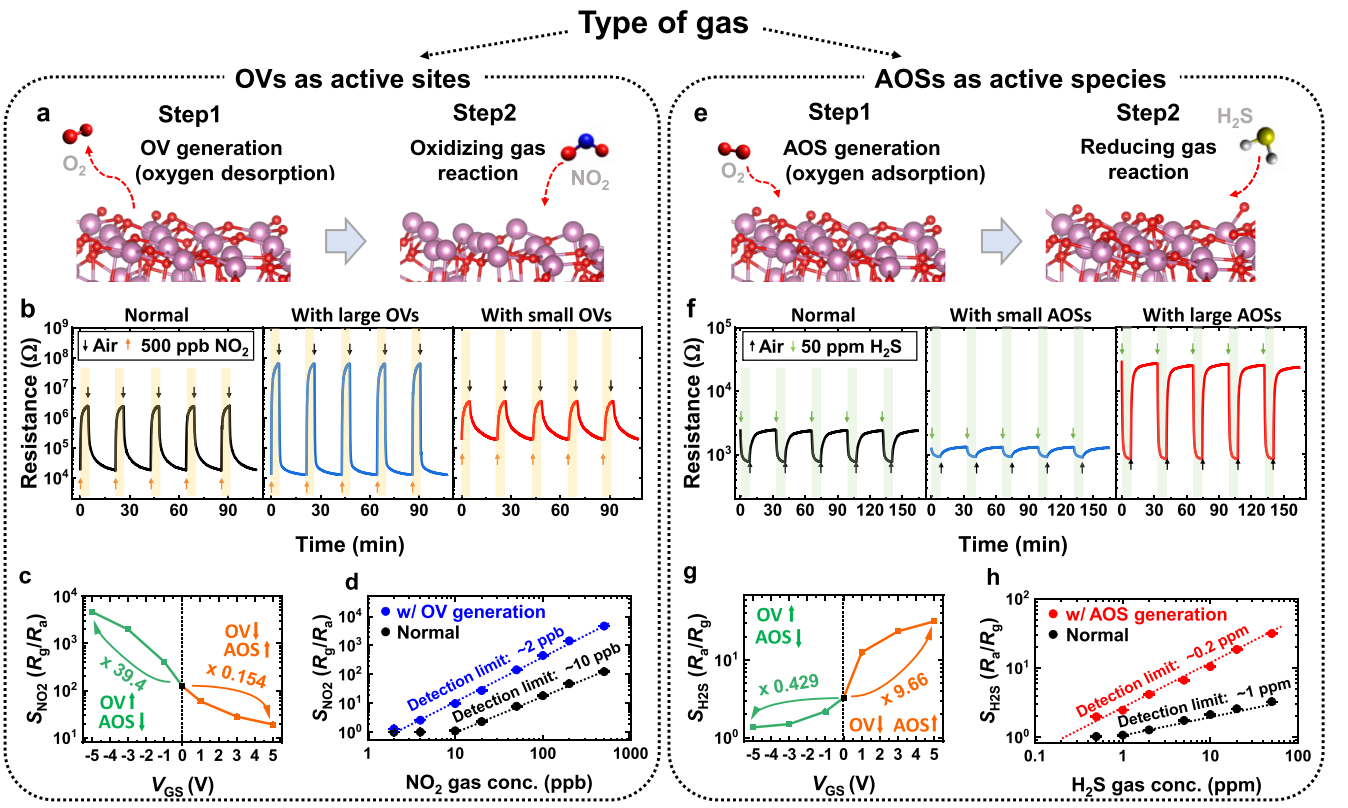

Figure 2. Effect of surface oxygen manipulation on the chemisorption in In_2O_3. (a) Schematic for surface oxygen manipulation of MOX to enhance the oxidizing gas reaction. (b) Response characteristics of the In_2O_3 gas sensor to 500 ppb NO_2 gas with and without oxygen manipulation method at 160 °C. From the left, these are the NO_2 gas response cyclic curves of the sensor without oxygen manipulation, with oxygen desorption, and with oxygen adsorption. (c) Steady-state responses (S_{NO2}) of In_2O_3 sensors to 500 ppb NO_2 gas at different levels of surface oxygen manipulation. (d) S_{NO2} versus NO_2 gas concentration with and without oxygen desorption. (e) Schematic for surface oxygen manipulation of MOX to enhance the reducing gas reaction. (f) Response characteristics of the In_2O_3 gas sensor to 50 ppm of H_2S gas with and without oxygen manipulation at 240 °C. From the left, these are the H_2S gas response cyclic curves of the sensor without oxygen manipulation, with oxygen desorption, and with oxygen adsorption. (g) Steady-state responses (S_{H2S}) of In_2O_3 sensors to 50 ppm of H_2S gas at different levels of surface oxygen manipulation. (h) S_{H2S} versus H_2S gas concentration with and without oxygen adsorption. S_{NO2} and S_{H2S} are measured five times, and the mean and one standard deviation are plotted using error bars.

XPS peaks of the In_2O_3 devices are analyzed considering the full width at half-maximum (fwhm, 1.85 eV) and the position (~532.3 eV) of the SiO_2 O_{1s} XPS peak. The O_{1s} XPS spectra originating from the In_2O_3 devices are deconvoluted into two bands at 529.7 and 531.6 eV. The low binding energy peak is attributed to the lattice oxygen of In_2O_3 (In−O). The high binding energy peak is related to oxygen vacancies and surface hydroxyl groups.[8,32,33] Many studies have claimed that oxygens near oxygen vacancies cause a peak around 531.6 eV.[7,8,34] However, recent studies claim that the peak originates from hydroxy groups (OH) because surface oxygen vacancies are rapidly converted to hydroxy groups by water vapor in the air.[33,35] Here, we focus on the proportion of the lattice oxygen. When oxygen adsorption and desorption processes are performed on pristine indium oxide, the amount of O−In increases and decreases, respectively, relative to the pristine state (Table S1). The In $3d_{5/2}$ and $3d_{3/2}$ core level XPS spectra are each deconvoluted into two bands (Figure 1(c)), respectively. High energy peaks at 444.7 eV ($3d_{5/2}$) and 452.2 eV ($3d_{3/2}$) are attributed to indium, which is completely complemented by oxygens. Conversely, lower binding energy peaks at 444 ($3d_{5/2}$) and 451.5 eV ($3d_{3/2}$) are related to the surface hydroxy group and oxygen vacancies.[36] Oxygen adsorption and desorption processes on pristine indium oxide increase and decrease the amounts of In and O that are perfectly complementary to one another (Table S2).

To further validate the functionality of the proposed method, changes in the electrical resistance of In_2O_3 are examined. The proposed method is applied in atmospheric (760 Torr) and low-oxygen environments (10^{-2} Torr). In the low-oxygen environment, the oxygen adsorption method results in less oxygen adsorption and resistance change than in the atmospheric environment (Figure 1(d)). However, the oxygen desorption method in a low-oxygen environment allows more oxygen desorption (Figure 1(e)). This indicates that the resistance change of In_2O_3 is a result of the interaction between oxygen in air and In_2O_3. Increasing the gate voltage to regulate the carrier concentration resulted in a greater resistance change in all cases. Based on the above results, we can deduce that by changing the electron concentration of MOX using the proposed method, the surface reaches a new equilibrium by interacting with oxygen in the environment; in this new equilibrium, oxygen concentration on the surface is manipulated.

First-principles calculations based on DFT are performed to verify the surface oxygen control method. By variation of the In_2O_3 electron concentration, the binding energy (ΔE) of oxygen is calculated. As expected, when the electron concentration increases, ΔE decreases, and oxygen adsorption

https://doi.org/10.1021/acsnano.3c03034
ACS Nano 2023, 17, 17790−17798

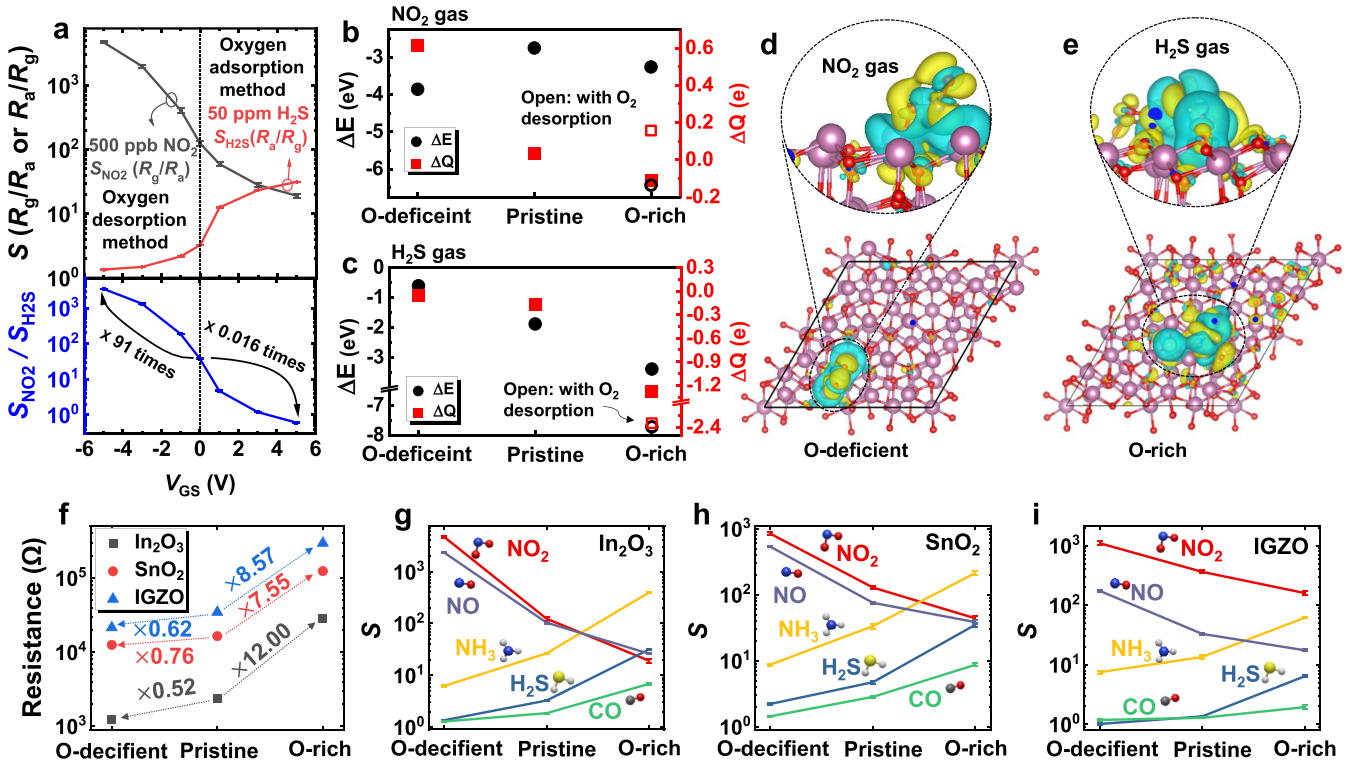

Figure 3. Effects of surface oxygen manipulation on gas selectivity of sensors. (a) S_{NO2}, S_{H2S}, and S_{NO2}/S_{H2S} of In_2O_3 sensors for 500 ppb of NO_2 gas and 50 ppm of H_2S gas with different levels of surface oxygen manipulation. Charge transfer (ΔQ) and adsorption energy (ΔE) values of (b) NO_2 and (c) H_2S gases on O-deficient, pristine, and O-rich In_2O_3 (111) surfaces. Bader charge analysis of (d) NO_2 and (e) H_2S gas adsorption on (d) O-deficient and (e) -rich In_2O_3 surfaces, respectively. The blue and yellow charge distributions represent the positive and negative electron density changes after gas adsorption, respectively. (f) Changes in electrical resistances caused by applying surface oxygen manipulation to In_2O_3, SnO_2, and IGZO. S of the gases (500 ppb of NO_2, 500 ppb of NO, 50 ppm of H_2S, 100 ppm of NH_3, and 100 ppm of CO) with and without the surface oxygen manipulation in (g) In_2O_3, (h) SnO_2, and (i) IGZO.

is promoted. When the electron concentration decreases, ΔE becomes positive, and oxygen desorption occurs. Controlling the concentration of surface electrons affects the oxygen adsorption energy, which determines the surface oxygen concentration.

Effect on Chemisorption. In many redox reactions related to MOXs, OVs are representative active sites traditionally used,[37] and AOSs are the active species based on the generally accepted Mars–van Krevelen (MvK) mechanism.[12,13,38] Facilitating oxygen adsorption with the proposed method reduces surface OVs and increases AOSs, whereas promoting oxygen desorption produces the opposite effect. We find that the oxidizing gases use OVs as the active sites. In contrast, reducing gases utilize AOSs as active species. Using the proposed method, the MOX can be controlled to react primarily with specific types of gases (reducing or oxidizing gas). We verified the gas selectivity using the gas sensing signals of the fabricated devices.

As the OVs increase due to the desorption of surface oxygen, the adsorption of oxidizing gases (e.g., NO_2) and the signal of the fabricated sensor increase (Figure 2(a)). After the oxygen desorption step, the In_2O_3 sensors show 39.4-times larger responses (S_{NO2}) to 500 ppb of NO_2 gas than without the step (Figure 2(b) and (c)). In contrast, after the oxygen adsorption step, S_{NO2} decreases by 0.154-times relative to the value without the step. Increasing the amount of oxygen adsorption and desorption increases the efficacy of oxygen control (Figure 2(c)). The oxygen desorption method allows more NO_2 gas to be adsorbed and increases the charge transfer, significantly reducing the detection limit of the sensor (Figure 2(d)). Without oxygen desorption, the sensor detects up to 10 ppb of NO_2 gas; with oxygen desorption, the sensor responds to even small amounts of gas, allowing the same sensor to detect up to 2 ppb of NO_2 gas (~5-times lower).

In contrast to the oxidizing gas, the quantity of reducing gas (e.g., H_2S gas) reaction and the magnitude of the sensor signal rise as the amount of AOS increases (Figure 2(e)). The oxygen adsorption step enhances the H_2S gas response (S_{H2S}) by 9.66-times relative to the value before performing the step (Figure 2(f) and (g)). In addition, oxygen adsorption reduces the H_2S detection limit from 1 to 0.2 ppm. Conversely, if oxygen desorption occurs, OVs increase, AOSs decrease, and S_{H2S} decreases to ~1.35, making the In_2O_3 surface insensitive to H_2S gas. Controlling the amount of surface oxygen has opposite impacts on the NO_2 and H_2S gas reactions. The surface oxygen control allows In_2O_3 to be reconfigured to have selectivity for certain types of gases. When the oxygen desorption method is used, S_{NO2} increases, while S_{H2S} decreases, increasing S_{NO2}/S_{H2S} from 38 to 3457. In contrast, when oxygen adsorption is used, S_{NO2}/S_{H2S} decreases to 0.6 (Figure 3(a)).

The temperature and time of the oxygen manipulation method affect the surface oxygen contents, S_{NO2}, and S_{H2S}. As the oxygen manipulation temperature increases from 120 to 360 °C, the manipulation effect increases, and both S_{NO2} and S_{H2S} increase (Figure S3). Similarly, S_{NO2} and S_{H2S} increase with increasing manipulation time (Figure S4). Due to the fact that S_{NO2} and S_{H2S} increase substantially even after a brief period of

https://doi.org/10.1021/acsnano.3c03034
ACS Nano 2023, 17, 17790–17798

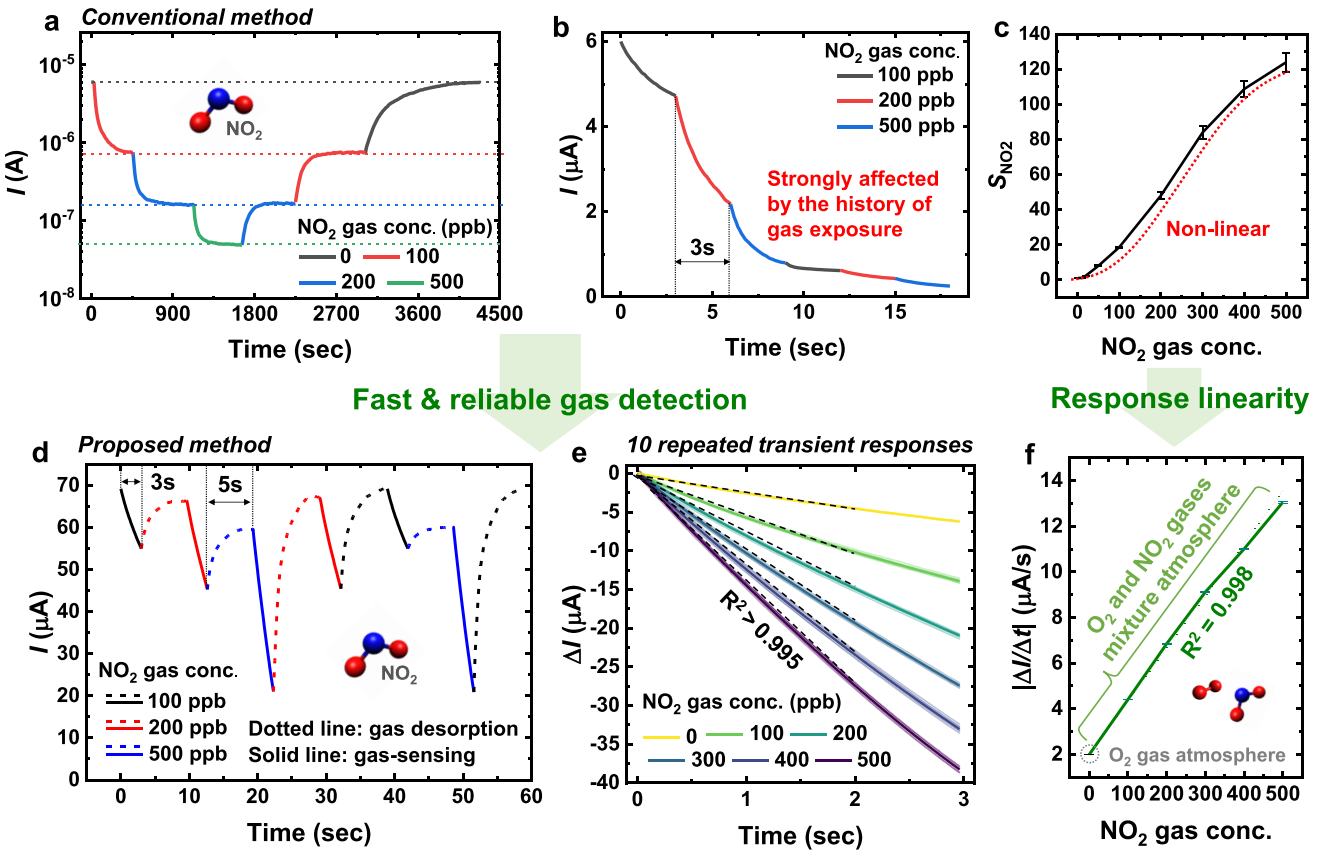

Figure 4. Comparison of NO_2 gas concentration identification with and without surface oxygen manipulation. (a) Conventional method for identifying gas concentration using steady-state responses. (b) Conventional problem with identifying gas concentrations using transient responses. (c) Nonlinearity of the steady-state response to gas concentration due to intrinsic properties. (d) Fast and reliable gas concentration identification by performing gas desorption before gas sensing. (e) Current changes (ΔI) in transient responses of the sensor to 0−500 ppb of NO_2 gas obtained after conducting gas desorption. Ten transient responses from each of the six gas concentrations and their average values are shown as transparent and solid lines, respectively. (f) Slopes of transient responses ($\Delta I/\Delta t$) in various environments where oxygen and NO_2 gas are mixed. The mean and one standard deviation of ten $\Delta I/\Delta t$s obtained at each concentration are displayed using error bars.

manipulation time, it is recommended to apply an appropriate manipulation time for sensor application considering the power consumption.

To explain the experimental data, we calculate the ΔE and charge transfer values (ΔQ) of NO_2 and H_2S gases to pristine, oxygen-rich, and oxygen-deficient In_2O_3 surfaces by using DFT. Figure S5 depicts various In_2O_3 surfaces utilized in the DFT computations. On the O-deficient In_2O_3 surface, relative to the pristine surface, the ΔE of NO_2 increases in the negative direction, while the ΔE of H_2S increases in the positive direction (Figure 3(b) and (c)). In contrast, when the pristine surface becomes O-rich, the ΔE of both NO_2 and H_2S gases increases in the negative direction. In addition, when oxygen gas is desorbed because of gas adsorption, ΔE increases in a more negative direction (open circles in Figure 3(b) and (c)). In the case of NO_2, $|\Delta E|$ is the largest when the O of NO_2 is combined with In at the OV site. Conversely, H_2S gas molecules have the largest $|\Delta E|$ when combined with the AOS of In_2O_3.

The change in electron charge density during NO_2/H_2S gas adsorption is calculated to quantify the charge transfer between NO_2/H_2S gas and In_2O_3 (Figures 3(b)−(e) and S6, and Tables S3 and S4). The ΔQs of the In_2O_3 surface are 0.034e for the pristine surface and 0.614e (18-times larger) for the O-deficient surface (Figure 3(d)). This result explains why the NO_2 gas-sensing properties (detection limit and S_{NO2}) improve after oxygen desorption. When NO_2 gas is adsorbed on an O-rich surface, the sign of ΔQ for the surface differs depending on whether oxygen is additionally desorbed. When oxygen is additionally desorbed from the surface, the ΔQ is 0.157e; when oxygen is not desorbed, the ΔQ is −0.110e. The ΔQ due to H_2S gas adsorption on the O-deficient surface is −0.054e, which is 3.2-times less than that on the pristine surface. In contrast, on the O-rich surface, ΔQ is significantly more negative than that on the pristine surface, regardless of whether oxygen is desorbed (Figure 3(c)). On the O-deficient surface, H_2S gas is less adsorbed and has less impact on the sensor signal; on the O-rich surface, more H_2S gas is adsorbed and exhibits a more significant effect on the sensor signal.

The applicability of the proposed method to other MOXs (SnO_2 and IGZO) is evaluated (Figure 3(f)−(i)). Using the proposed method, the surface oxygen content of SnO_2 and IGZO is manipulated (Figure 3f). The effect of surface oxygen manipulation on the chemisorption of oxidizing (NO, NO_2) and reducing (H_2S, NH_3, and CO) gases is tested (Figure 3(g)−(i)). In all three MOXs, the reaction of oxidizing gases increases as the quantity of OV grows, while the reaction of reducing gases increases as the amount of AOS increases.

The amount of OV and AOS on the surface of the MOX may change over time or with gaseous reactions.[39,40] Our manipulation approach effectively returns the MOX surface to

https://doi.org/10.1021/acsnano.3c03034
ACS Nano 2023, 17, 17790−17798

its desired condition by utilizing ubiquitous oxygen. This uniformity of the MOX enables a consistent amount of chemisorption regardless of previous gas reactions. Preceding the manipulation method to the gas reaction allowed almost identical amounts of chemisorption and gas response over a long period (Figure S7). Note that the proposed method exhibits much less variation in sensor response over time compared with the most popular existing preheating method presented in commercial sensor manuals (Figure S7).

Application to Gas Sensors. Gas sensors convert the surface gas reaction into an electrical signal. Most of the existing MOX-based gas sensors utilize a steady-state response (Figure 4(a)). This response is trustworthy, since the same response is produced independently of the gas reaction history; however, obtaining the response requires significant time and energy. Therefore, attempts have been made to utilize transient responses to identify gases rapidly. However, identifying gases using transient responses is difficult because the transient response is highly dependent on the gas exposure history (Figure 4(b)).[41] In addition, the steady-state response of MOX is nonlinear due to its intrinsic properties, as evidenced by the Langmuir and Brunauer–Emmett–Teller (BET) models (Figure 4(c)).[42]

We present a method for obtaining fast and stable transient responses by manipulating the In_2O_3 surface. Repeatable transient responses to NO_2 gas are obtained by preceding the gas desorption step over the gas-sensing step (Figure 4(d)). During the gas desorption step, the electron concentration of In_2O_3 decreases, the ΔE values of NO_2 and O_2 gases increase in a positive direction (Figures 1e and S8), and the quantities of adsorbed gases decrease. Due to the gas desorption step, the sensor detects the NO_2 gas with a uniform MOX surface and generates a nearly identical transient response regardless of the gas exposure history. Unlike the conventional method, our method does not recover the sensor by artificially exposing it to a clean atmosphere (dry air or N_2). Our method is tested in an environment similar to the real environment where NO_2 gas is present in the atmosphere. Surprisingly, ten transient responses with different gas response histories exhibit almost identical current changes (ΔI) (Figure 4(e)). We utilize ΔI and slope ($\Delta I/\Delta t$) because the initial current value can vary depending on the external environment (Figure S9). ΔI and $\Delta I/\Delta t$ show linear relationships with the NO_2 gas concentration (R^2 = 0.998, Figures 4(f) and S10).

After the gas desorption step, MOX has a small surface coverage and desorption is negligible compared to adsorption. Therefore, the adsorption rate can be expressed as follows:[43]

$$dN_{gas}/dt = \alpha P_{gas} N^* \quad (1)$$

where α, N_{gas}, and N^* are the adsorption constant, the number of adsorbates, and adsorption centers per unit surface area, respectively. As long as desorption is negligible, the amount of adsorbed gas is proportional to the gas concentration (partial pressure). Due to the low surface coverage, the adsorption of the gas of O_2 and NO_2 can be regarded as a superposition of the adsorption of each gas. The $\Delta I/\Delta t$ is linear with the NO_2 gas concentration (Figure 4(f)). The proposed surface manipulation method enables rapid gas detection and minimizes the amount of energy consumption required for gas sensing.

Identifying precise gas concentrations in mixed-gas (oxidizing and reducing gases) environments has been considered a challenging task, because distinct gas concentration combinations produce the same sensor response (Figure 5(a)). In this

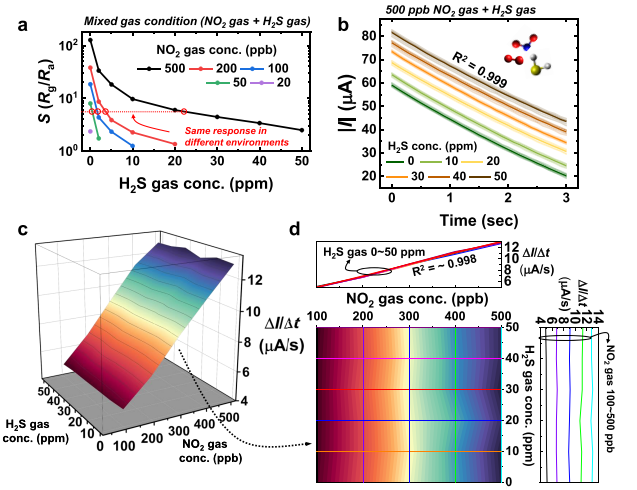

Figure 5. Linear responses in mixed-gas environments using oxygen manipulation. (a) Conventional steady-state responses to mixtures of NO_2 and H_2S gases at 160 °C. (b) Transient responses in mixed gas environments of 500 ppb of NO_2 with different concentrations of H_2S using oxygen desorption at 160 °C. (c) $\Delta I/\Delta t$ values in mixed gas settings with various combinations of NO_2 and H_2S gases. (d) $\Delta I/\Delta t$ versus NO_2 and H_2S gas concentrations in various mixed gas environments.

study, we demonstrate that by preceding with oxygen desorption, the sensor response can be made insensitive to H_2S gas while remaining sensitive to NO_2 gas. As shown in Figures 5(b) and S11, although the initial current value varies slightly with the H_2S concentration, $\Delta I/\Delta t$ hardly changes. Note that the ΔE of NO_2 gas on the O-deficient (OV-rich) surface is substantially more negative than that of H_2S; the $|\Delta Q|$ of NO_2 is much larger than that of H_2S (Figure 3(b) and (c)). By increasing the OVs and decreasing AOSs, the NO_2 gas reaction using OVs as active sites is promoted and the H_2S gas reaction using AOSs is suppressed. Figure 5(c) and (d) depict the $\Delta I/\Delta t$ values for various combinations of NO_2 and H_2S gas concentrations. Notably, $\Delta I/\Delta t$ shows a linear relationship with the NO_2 gas concentration; this parameter is unaffected by the H_2S gas concentration. Therefore, even in an environment containing both NO_2 and H_2S, the sensor accurately identifies the NO_2 gas concentration.

CONCLUSIONS

This work introduces a method for reconfigurable manipulation of MOX surfaces by electrically altering the electron concentration of MOX. Controlling the electron concentration manipulates the amounts of OV and AOS on the MOX surface by regulating the oxygen adsorption energy. The proposed method is implemented by fabricating devices embedding microheaters that can operate as a gate. The chemisorption of specific target gases can be increased by manipulating the surface OVs and AOSs. Our method is applied to the gas sensors. It overcomes the limitations of existing gas sensors, such as nonlinearity, gas cross-sensitivity, slow gas identification time, and long-term reliability, with great performance. Since the proposed method can be applied as long as it can simultaneously provide heat and electric field to the MOX, it is expected that the same results can be obtained with various alternative methods. We believe that our method can be widely applied in fields utilizing MOX surfaces.

https://doi.org/10.1021/acsnano.3c03034
ACS Nano 2023, 17, 17790–17798

METHODS

Device Fabrication. The devices were fabricated by using standard complementary metal-oxide-semiconductor (CMOS) fabrication processes. Figure S1 depicts schematics of the fabrication procedure. A 550 nm silicon oxide was grown by wet oxidation on 6 in. (100)-oriented *p*-type silicon wafers. A 350 nm thick *in situ* n^+ polycrystalline silicon was deposited by using a low-pressure chemical vapor deposition process and then patterned to form the microheater (gate). To avoid contamination, a passivation layer of SiO_2(10 nm)/Si_3N_4(20 nm)/SiO_2(10 nm) was deposited. The electrodes were fabricated by depositing and patterning metal layers (Ti (20 nm), TiN (20 nm), Al (70 nm), and TiN (20 nm) after forming contact holes. Under the device, an air gap was formed to minimize heat transfer from the microheater to the Si substrate. Using a radio frequency magnetron sputtering process, we deposited MOX (18 nm thick In_2O_3, 15 nm thick SnO_2, and 20 nm thick IGZO) films and patterned.

In_2O_3 Characterization. Point XPS data were obtained using a PHI VersaProbe III scanning XPS microprobe equipped with an Al Kα source. The resolution of the obtained point XPS was 10 μm × 10 μm, and the position of the device was found using a scanning X-ray image (SXI). The grazing incidence X-ray diffraction (GIXRD) data were obtained using an Xpert Pro (PANalytical).

Surface Oxygen Control Method. The surface oxygen control method was performed by applying the appropriate voltages to both ends of a heater. The temperature of the device was increased through the voltage difference across the heater; the gate bias application effect was obtained by increasing or decreasing both voltages applied to the ends, while maintaining the voltage difference across the heater. The surface oxygen control method was deliberately performed long enough (10 min) at 240 °C to see its effect clearly. During fast gas identification using linear response, the oxygen control step was performed at 160 °C for 5 s in both NO_2 gas and mixed-gas atmosphere. Both resistor terminals (source and drain) were grounded. The oxygen adsorption and desorption processes were performed at V_{GS} = 5 and −5 V, respectively. The temperature of the microheater was obtained using a resistance temperature detection method.[44]

Sensor Data Measurement. The sensor data were collected by using a probe station with the capacity for gas injection and ejection and a semiconductor parameter analyzer (B1500A, Agilent). The target gas was injected into the chamber at a rate of 200 mL/min after the concentration was adjusted in a homemade mixing chamber using a reference gas (air). 100−500 ppb NO_2, 10−50 ppm of H_2S, 500 ppb NO, 100 ppm of CO, and 100 ppm of NH_3 were used as target gases. The sensor was operated at 160 and 240 °C for NO_2 and NO gases and H_2S, NH_3, and CO gases reaction, respectively. The sensor was operated at 160 °C in the environment where the two gases (NO_2 + H_2S) were mixed. The steady-state responses of the sensor (S) were determined using the resistance ratio before and after the gas response; these values were calculated as follows.

$$S_{NO2},\ S_{NO} = R_g/R_a \tag{2}$$

$$S_{H2S},\ S_{CO},\ \text{and}\ S_{NH3} = R_a/R_g \tag{3}$$

where R_a and R_g denote the sensor resistance levels in air and the target gas, respectively. The mean and standard deviation values of the responses from five repeated gas reactions are shown using error bars. In the conventional preheating method used for long-term reliability comparison, the gas sensor was heated to the same temperature as the gas reaction temperature for 1 h in dry air before the gas reaction.

Computational Details. DFT calculations were performed on an In_2O_3 (111) surface based on the GIXRD pattern of the indium oxide film (Figure S12); this surface was chosen because the (111) surface is the most thermodynamically favored termination surface.[45] DFT calculations were conducted using the Vienna *Ab initio* Simulation Package (VASP).[46] The Perdew−Burke−Ernzerhof (PBE) exchange-correlation functional based on the generalized gradient approximation (GGA) was implemented.[47] The cutoff energy for the plane-wave basis set was chosen as 450 eV, and spin-polarized calculations were performed for all structures. The slab structure contained 48 In_2O_3 units (240 atoms in total) with six O−In−O layers. The bottom three layers were fixed to reduce the computational cost. For O-rich and O-deficient structures, single monolayers of O atoms were added and removed from the pristine structures, respectively. For all slab structures, a vacuum of 15 was applied to avoid interactions between layers due to periodic boundary conditions. For the binding of H_2S and NO_2 molecules, 18 different sites were considered for the calculations. The binding energy (ΔE) values of the adsorbates were calculated by the following equation:

$$\Delta E = E(*X) - E(*) - E(X) \tag{4}$$

where X is the adsorbate molecule, $E(*X)$ and $E(*)$ are the total energies of the surface with and without X, respectively, and $E(X)$ is the total energy of X. Bader charge analysis was performed with code from Henkelman Group to obtain the charge transfer characteristics between the surfaces and adsorbates.[48] The differences in charge values from Bader charge analysis and the number of valence electrons in pseudopotential files represent the oxidation states. The charge density difference plot was obtained by the following equation:

$$\Delta\rho = \rho(*X) - \rho(*) - \rho(X) \tag{5}$$

where X is the adsorbate molecule, $\rho(*X)$ and $\rho(*)$ are the charge densities of the surface with and without X, respectively, and $\rho(X)$ is the charge density of X. Structures with different electron densities were simulated by changing the number of electrons (NELECT) parameter of the VASP program. The NELECT tag determined the number of valence electrons in the system. From the default values of NELECT, values were increased or decreased by two to generate systems with larger or smaller electron densities, respectively.

ASSOCIATED CONTENT

Supporting Information

The Supporting Information is available free of charge at https://pubs.acs.org/doi/10.1021/acsnano.3c03034.

Fabrication processes of MOX devices; SEM and EDS mapping images of the device; Response characteristics of an In_2O_3 gas sensor as a function of oxygen manipulation temperature and time; Various In_2O_3 slabs for DFT calculations; Bader charge analyses of NO_2 and H_2S gas adsorption on the In_2O_3 (111) surface; Steady-state response of the sensor over time; Binding energy (ΔE) values of NO_2 at different In_2O_3 electron concentration; Transient responses of the sensors with gas desorption method; ΔI versus NO_2 gas concentration; GIXRD pattern; Area ratio of XPS peaks; Bader charge analyses (PDF)

AUTHOR INFORMATION

Corresponding Author

Jong-Ho Lee − *Department of Electrical and Computer Engineering and Inter-university Semiconductor Research Center, Seoul National University, Seoul 08826, Republic of Korea; Ministry of Science and ICT, Sejong 30121, Republic of Korea;* orcid.org/0000-0003-3559-9802; Phone: +82-2-880-1727; Email: jhl@snu.ac.kr; Fax: +82-2-882-4658

Authors

Gyuweon Jung − *Department of Electrical and Computer Engineering and Inter-university Semiconductor Research Center, Seoul National University, Seoul 08826, Republic of Korea;* orcid.org/0000-0003-0357-0933

Suyeon Ju − *Department of Materials Science and Engineering and Research Institute of Advanced Materials, Seoul National University, Seoul 08826, Republic of Korea;* orcid.org/0000-0001-7033-8769

https://doi.org/10.1021/acsnano.3c03034
ACS Nano 2023, 17, 17790−17798

Kangwook Choi − *Department of Electrical and Computer Engineering and Inter-university Semiconductor Research Center, Seoul National University, Seoul 08826, Republic of Korea*

Jaehyeon Kim − *Department of Electrical and Computer Engineering and Inter-university Semiconductor Research Center, Seoul National University, Seoul 08826, Republic of Korea*

Seongbin Hong − *Department of Electrical and Computer Engineering and Inter-university Semiconductor Research Center, Seoul National University, Seoul 08826, Republic of Korea;* orcid.org/0000-0002-6719-7608

Jinwoo Park − *Department of Electrical and Computer Engineering and Inter-university Semiconductor Research Center, Seoul National University, Seoul 08826, Republic of Korea*

Wonjun Shin − *Department of Electrical and Computer Engineering and Inter-university Semiconductor Research Center, Seoul National University, Seoul 08826, Republic of Korea*

Yujeong Jeong − *Department of Electrical and Computer Engineering and Inter-university Semiconductor Research Center, Seoul National University, Seoul 08826, Republic of Korea*

Seungwu Han − *Department of Materials Science and Engineering and Research Institute of Advanced Materials, Seoul National University, Seoul 08826, Republic of Korea;* orcid.org/0000-0003-3958-0922

Woo Young Choi − *Department of Electrical and Computer Engineering and Inter-university Semiconductor Research Center, Seoul National University, Seoul 08826, Republic of Korea*

Complete contact information is available at: https://pubs.acs.org/10.1021/acsnano.3c03034

Author Contributions

G.J. and J.-H.L. conceived and led the research. S.J. and S.W.H. contributed to the DFT simulations. G.J. and S.B.H. contributed to the device fabrication. G.J., K.C., and J.K. contributed to data acquisition. G.J. and J.P. contributed to the reliability measurements. W.S. and Y.J. contributed to the data analysis. G.J. and J.-H.L. cowrite the paper. S.W.H., W.Y.C., and J.-H.L. contributed to the supervision. All authors discussed the results and commented on the manuscript.

Notes

The authors declare no competing financial interest.

ACKNOWLEDGMENTS

This work was supported by the BK21 FOUR program of the Education and Research Program for Future ICT Pioneers, Seoul National University, in 2023, and the National Research Foundation of Korea (2021R1A2C3009069).

ABBREVIATIONS

MOX, metal oxide; OV, oxygen vacancy; AOS, adsorbed oxygen species; DFT, density functional theory; XPS, X-ray photoelectron spectroscopy; GIXRD, glazing incidence X-ray diffraction; SEM, scanning electron microscopy

REFERENCES

(1) Li, H.; Kelly, S.; Guevarra, D.; Wang, Z.; Wang, Y.; Haber, J. A.; Anand, M.; Gunasooriya, G. T. K. K.; Abraham, C. S.; Vijay, S.; Gregoire, J. M.; Nørskov, J. K. Analysis of the Limitations in the Oxygen Reduction Activity of Transition Metal Oxide Surfaces. *Nature Catalysis 2021 4:6* **2021**, *4* (6), 463−468.

(2) Yang, J. J.; Pickett, M. D.; Li, X.; Ohlberg, D. A. A.; Stewart, D. R.; Williams, R. S. Memristive Switching Mechanism for Metal/Oxide/Metal Nanodevices. *Nature Nanotechnology 2008 3:7* **2008**, *3* (7), 429−433.

(3) Xu, A.; Hung, S. F.; Cao, A.; Wang, Z.; Karmodak, N.; Huang, J. E.; Yan, Y.; Sedighian Rasouli, A.; Ozden, A.; Wu, F. Y.; Lin, Z. Y.; Tsai, H. J.; Lee, T. J.; Li, F.; Luo, M.; Wang, Y.; Wang, X.; Abed, J.; Wang, Z.; Nam, D. H.; Li, Y. C.; Ip, A. H.; Sinton, D.; Dong, C.; Sargent, E. H. Copper/Alkaline Earth Metal Oxide Interfaces for Electrochemical CO2-to-Alcohol Conversion by Selective Hydrogenation. *Nature Catalysis 2022 5:12* **2022**, *5* (12), 1081−1088.

(4) Park, J. S.; Kim, S.; Xie, Z.; Walsh, A. Point Defect Engineering in Thin-Film Solar Cells. *Nature Reviews Materials* **2018**, *3*, 194.

(5) Wang, G.; Yang, Y.; Han, D.; Li, Y. Oxygen Defective Metal Oxides for Energy Conversion and Storage. *Nano Today* **2017**, *13*, 23−39.

(6) Potyrailo, R. A.; Go, S.; Sexton, D.; Li, X.; Alkadi, N.; Kolmakov, A.; Amm, B.; St-Pierre, R.; Scherer, B.; Nayeri, M.; Wu, G.; Collazo-Davila, C.; Forman, D.; Calvert, C.; Mack, C.; McConnell, P. Extraordinary Performance of Semiconducting Metal Oxide Gas Sensors Using Dielectric Excitation. *Nat. Electron* **2020**, *3* (5), 280−289.

(7) Qi, Y.; Song, L.; Ouyang, S.; Liang, X.; Ning, S.; Zhang, Q.; Ye, J. Photoinduced Defect Engineering: Enhanced Photothermal Catalytic Performance of 2D Black In2O3−x Nanosheets with Bifunctional Oxygen Vacancies. *Adv. Mater.* **2020**, *32* (6), 1903915.

(8) Wei, W.; Wei, Z.; Li, R.; Li, Z.; Shi, R.; Ouyang, S.; Qi, Y.; Philips, D. L.; Yuan, H. Subsurface Oxygen Defects Electronically Interacting with Active Sites on In2O3 for Enhanced Photothermocatalytic CO2 Reduction. *Nature Communications 2022 13:1* **2022**, *13* (1), 1−12.

(9) Zhang, C.; Liu, G.; Geng, X.; Wu, K.; Debliquy, M. Metal Oxide Semiconductors with Highly Concentrated Oxygen Vacancies for Gas Sensing Materials: A Review. *Sensors and Actuators, A: Physical* **2020**, *309*, 112026.

(10) Al-Hashem, M.; Akbar, S.; Morris, P. Role of Oxygen Vacancies in Nanostructured Metal-Oxide Gas Sensors: A Review. *Sens Actuators B Chem.* **2019**, *301*, 126845.

(11) Linsebigler, A.; Lu, G.; Yates, J. T. CO Chemisorption on TiO2(110): Oxygen Vacancy Site Influence on CO Adsorption. *J. Chem. Phys.* **1995**, *103* (21), 9438.

(12) Gurlo, A. Interplay between O2 and SnO2: Oxygen Ionosorption and Spectroscopic Evidence for Adsorbed Oxygen. *ChemPhysChem* **2006**, *7* (10), 2041−2052.

(13) Blackman, C. Do We Need Ionosorbed" Oxygen Species? (Or, "a Surface Conductivity Model of Gas Sensitivity in Metal Oxides Based on Variable Surface Oxygen Vacancy Concentration"). *ACS Sensors* **2021**, 3509−3516, DOI: 10.1021/acssensors.1c01727.

(14) Wu, J.; Li, X.; Shi, W.; Ling, P.; Sun, Y.; Jiao, X.; Gao, S.; Liang, L.; Xu, J.; Yan, W.; Wang, C.; Xie, Y. Efficient Visible-Light-Driven CO2 Reduction Mediated by Defect-Engineered BiOBr Atomic Layers. *Angewandte Chemie - International Edition* **2018**, *57* (28), 8719.

(15) Tong, Y.; Chen, P.; Zhang, M.; Zhou, T.; Zhang, L.; Chu, W.; Wu, C.; Xie, Y. Oxygen Vacancies Confined in Nickel Molybdenum Oxide Porous Nanosheets for Promoted Electrocatalytic Urea Oxidation. *ACS Catal.* **2018**, *8* (1), 1.

(16) Setvín, M.; Aschauer, U.; Scheiber, P.; Li, Y. F.; Hou, W.; Schmid, M.; Selloni, A.; Diebold, U. Erratum: Reaction of O2 with Subsurface Oxygen Vacancies on TiO2 Anatase (101). *Science* **2015**, *349*, aac9659.

(17) Zhuang, G.; Chen, Y.; Zhuang, Z.; Yu, Y.; Yu, J. Oxygen Vacancies in Metal Oxides: Recent Progress towards Advanced Catalyst Design. *Science China Materials* **2020**, *63*, 2089.

(18) Wang, Z.; Lin, R.; Huo, Y.; Li, H.; Wang, L. Formation, Detection, and Function of Oxygen Vacancy in Metal Oxides for Solar Energy Conversion. *Adv. Funct. Mater.* **2022**, *32*, 2109503.

(19) Dvořák, F.; Szabová, L.; Johánek, V.; Farnesi Camellone, M.; Stetsovych, V.; Vorokhta, M.; Tovt, A.; Skála, T.; Matolínová, I.; Tateyama, Y.; Mysliveček, J.; Fabris, S.; Matolín, V. Bulk Hydroxylation

and Effective Water Splitting by Highly Reduced Cerium Oxide: The Role of O Vacancy Coordination. *ACS Catal.* **2018**, *8* (5), 4354.
(20) Frei, M. S.; Mondelli, C.; García-Muelas, R.; Morales-Vidal, J.; Philipp, M.; Safonova, O. v.; López, N.; Stewart, J. A.; Ferré, D. C.; Pérez-Ramírez, J. Nanostructure of Nickel-Promoted Indium Oxide Catalysts Drives Selectivity in CO2 Hydrogenation. *Nature Communications 2021 12:1* **2021**, *12* (1), 1−9.
(21) Amini, K.; Gostick, J.; Pritzker, M. D. Metal and Metal Oxide Electrocatalysts for Redox Flow Batteries. *Adv. Funct. Mater.* **2020**, *30*, 1910564.
(22) Yu, K.; Lou, L. L.; Liu, S.; Zhou, W. Asymmetric Oxygen Vacancies: The Intrinsic Redox Active Sites in Metal Oxide Catalysts. *Advanced Science* **2020**, *7*, 1901970.
(23) Grimaud, A.; Diaz-Morales, O.; Han, B.; Hong, W. T.; Lee, Y. L.; Giordano, L.; Stoerzinger, K. A.; Koper, M. T. M.; Shao-Horn, Y. Activating Lattice Oxygen Redox Reactions in Metal Oxides to Catalyse Oxygen Evolution. *Nat. Chem.* **2017**, *9* (5), 457.
(24) Jung, G.; Hong, S.; Jeong, Y.; Shin, W.; Park, J.; Kim, D.; Lee, J.-H. Highly Selective and Low-Power Carbon Monoxide Gas Sensor Based on the Chain Reaction of Oxygen and Carbon Monoxide to WO 3. *ACS Appl. Mater. Interfaces* **2022**, *14*, 33.
(25) Wetchakun, K.; Samerjai, T.; Tamaekong, N.; Liewhiran, C.; Siriwong, C.; Kruefu, V.; Wisitsoraat, A.; Tuantranont, A.; Phanichphant, S. Semiconducting Metal Oxides as Sensors for Environmentally Hazardous Gases. *Sens Actuators B Chem.* **2011**, *160* (1), 580.
(26) Lee, S.; Kim, S.; Nam, G. B.; Eom, T. H.; Jang, H. W. Chemoresistive Gas Sensors for Food Quality Monitoring. *Journal of Semiconductor Technology and Science* **2022**, *22* (4), 244.
(27) Kim, T.; Lee, T. H.; Park, S. Y.; Eom, T. H.; Cho, I.; Kim, Y.; Kim, C.; Lee, S. A.; Choi, M. J.; Suh, J. M.; Hwang, I. S.; Lee, D.; Park, I.; Jang, H. W. Drastic Gas Sensing Selectivity in 2-Dimensional MoS2 Nanoflakes by Noble Metal Decoration. *ACS Nano* **2023**, *17*, 4404.
(28) Park, S. Y.; Kim, Y.; Kim, T.; Eom, T. H.; Kim, S. Y.; Jang, H. W. Chemoresistive Materials for Electronic Nose: Progress, Perspectives, and Challenges. *InfoMat* **2019**, *1*, 289.
(29) Covington, J. A.; Marco, S.; Persaud, K. C.; Schiffman, S. S.; Nagle, H. T. Artificial Olfaction in the 21stCentury. *IEEE Sensors Journal* **2021**, *21*, 12969.
(30) Dey, A. Semiconductor Metal Oxide Gas Sensors: A Review. *Materials Science and Engineering: B* **2018**, *229*, 206−217.
(31) Shin, H.; Kim, D. H.; Jung, W.; Jang, J. S.; Kim, Y. H.; Lee, Y.; Chang, K.; Lee, J.; Park, J.; Namkoong, K.; Kim, I. D. Surface Activity-Tuned Metal Oxide Chemiresistor: Toward Direct and Quantitative Halitosis Diagnosis. *ACS Nano* **2021**, *15* (9), 14207−14217.
(32) Hashemi, A.; Bahari, A. Structural and Dielectric Characteristic of Povidone−Silica Nanocomposite Films on the Si (n) Substrate. *Appl. Phys. A Mater. Sci. Process* **2017**, *123* (8), 1−7.
(33) Idriss, H. On the Wrong Assignment of the XPS O1s Signal at 531−532 EV Attributed to Oxygen Vacancies in Photo- and Electro-Catalysts for Water Splitting and Other Materials Applications. *Surf. Sci.* **2021**, *712*, 121894.
(34) Jung, G.; Shin, H.; Jeon, S. W.; Lim, Y. H.; Hong, S.; Kim, D. H.; Lee, J. H. Transducer-Aware Hydroxy-Rich-Surface Indium Oxide Gas Sensor for Low-Power and High-Sensitivity NO2 Gas Sensing. *ACS Appl. Mater. Interfaces* **2023**, *15*, 22651.
(35) Detweiler, Z. M.; Wulfsberg, S. M.; Frith, M. G.; Bocarsly, A. B.; Bernasek, S. L. The Oxidation and Surface Speciation of Indium and Indium Oxides Exposed to Atmospheric Oxidants. *Surf. Sci.* **2016**, *648*, 188.
(36) Kyndiah, A.; Ablat, A.; Guyot-Reeb, S.; Schultz, T.; Zu, F.; Koch, N.; Amsalem, P.; Chiodini, S.; Yilmaz Alic, T.; Topal, Y.; Kus, M.; Hirsch, L.; Fasquel, S.; Abbas, M. A Multifunctional Interlayer for Solution Processed High Performance Indium Oxide Transistors. *Sci. Rep* **2018**, *8* (1), 10946 DOI: 10.1038/s41598-018-29220-0.
(37) Over, H.; Kim, Y. D.; Seitsonen, A. P.; Wendt, S.; Lundgren, E.; Schmid, M.; Varga, P.; Morgante, A.; Ertl, G. Atomic-Scale Structure and Catalytic Reactivity of the RuO2(110) Surface. *Science (1979)* **2000**, *287* (5457), 1474−1476.
(38) Mars, P.; van Krevelen, D. W. Oxidations Carried out by Means of Vanadium Oxide Catalysts. *Chem. Eng. Sci.* **1954**, *3*, 41.
(39) Zhou, X.; Shen, Q.; Yuan, K.; Yang, W.; Chen, Q.; Geng, Z.; Zhang, J.; Shao, X.; Chen, W.; Xu, G.; Yang, X.; Wu, K. Unraveling Charge State of Supported Au Single-Atoms during CO Oxidation. *J. Am. Chem. Soc.* **2018**, *140* (2), 554.
(40) Selcuk, S.; Zhao, X.; Selloni, A. Structural Evolution of Titanium Dioxide during Reduction in High-Pressure Hydrogen. *Nat. Mater.* **2018**, *17* (10), 923.
(41) Satterthwaite, P. F.; Eberle, S.; Nedelcu, S.; Roman, C.; Hierold, C. Transient and Steady-State Readout of Nanowire Gas Sensors in the Presence of Low-Frequency Noise. *Sens Actuators B Chem.* **2019**, *297*, 126674.
(42) Yuan, C.; Ma, J.; Zou, Y.; Li, G.; Xu, H.; Sysoev, V. V.; Cheng, X.; Deng, Y. Modeling Interfacial Interaction between Gas Molecules and Semiconductor Metal Oxides: A New View Angle on Gas Sensing. *Advanced Science* **2022**, *9*, 2203594.
(43) Wolkenstein, T. *Electronic Processes on Semiconductor Surfaces during Chemisorption*; Springer Science & Business Media: New York, 2012.
(44) Jung, G.; Hong, Y.; Hong, S.; Jang, D.; Jeong, Y.; Shin, W.; Park, J.; Kim, D.; Jeong, C. B.; Kim, D. U.; Chang, K. S.; Lee, J. H. A Low-Power Embedded Poly-Si Micro-Heater for Gas Sensor Platform Based on a FET Transducer and Its Application for NO2 Sensing. *Sens Actuators B Chem.* **2021**, *334*, 129642.
(45) Walsh, A.; Catlow, C. R. A. Structure, Stability and Work Functions of the Low Index Surfaces of Pure Indium Oxide and Sn-Doped Indium Oxide (ITO) from Density Functional Theory. *J. Mater. Chem.* **2010**, *20* (46), 10438−10444.
(46) Kresse, G.; Furthmüller, J. Efficiency of Ab-Initio Total Energy Calculations for Metals and Semiconductors Using a Plane-Wave Basis Set. *Comput. Mater. Sci.* **1996**, *6* (1), 15−50.
(47) Perdew, J. P.; Burke, K.; Ernzerhof, M. Generalized Gradient Approximation Made Simple. *Phys. Rev. Lett.* **1996**, *77* (18), 3865.
(48) Tang, W; Sanville, E; Henkelman, G A Grid-Based Bader Analysis Algorithm without Lattice Bias. *J. Phys.: Condens. Matter* **2009**, *21* (8), 084204.

https://doi.org/10.1021/acsnano.3c03034
ACS Nano 2023, 17, 17790−17798